Supporting Information to

Propelling Polysulfide Redox Conversion by *d*-band modulation for High Sulfur Loading and Low Temperature Lithium-Sulfur Batteries

Pan Zeng,[1] Cheng Liu,[1] Chen Cheng,[1] Cheng Yuan,[1] Kehua Dai,[2] Jing Mao,[3] Lirong Zheng,[4] Jing Zhang,[4] Lo-Yueh Chang,[5] Shu-Chih Haw,[5] Ting-Shan Chan,[5] Haiping Lin,[1] and Liang Zhang*[1]*

1. Institute of Functional Nano & Soft Materials (FUNSOM), Jiangsu Key Laboratory for Carbon-Based Functional Materials & Devices, Soochow University, 199 Ren'ai Road, Suzhou 215123, China

2. College of Chemistry, Tianjin Normal University, Tianjin 300387, China

3. School of Materials Science and Engineering, Zhengzhou University, Zhengzhou 450001, China

4. Beijing Synchrotron Radiation Facility, Institute of High Energy Physics, Chinese Academy of Sciences, Beijing 100049, China

5. National Synchrotron Radiation Research Center, Hsinchu 30076, Taiwan

Email: liangzhang2019@suda.edu.cn (L.Z.); chan.ts@nsrrc.org.tw (T.S.C)

Experimental Section

Synthesis of Ni_3Fe@HPC-CNT: The Ni_3Fe@HPC-CNT composite was prepared using a simple sol-gel method. In a typical synthesis process, 0.75 mmol $Ni(NO_3)_2 \cdot 6H_2O$ (Aladdin, 99.99%) and 0.25 mmol $Fe(NO_3)_3 \cdot 9H_2O$ (Aladdin, 99.99%) were dissolved in 30 mL N, N-dimethylformamide (Aladdin, 99.95%) solutions containing 1 g terephthalic acid (Aldrich, 99.99%) and strongly stirred at 30 °C for 0.5 h. Then, 2 mL tetraethyl orthosilicate (TEOS, Aladdin, 99.99%) was slowly added into above prepared solutions, and the final mixture solutions were stirred for another 0.5 h at the same temperature. The obtained claybank solutions were then heated at 40 °C and 80 °C for 36 h in an oven, respectively, for the thermopolymerization and sol-gel process. After heating of 72 h in an oven, the black gel was formed. It was then carbonized at 900 °C for 3 h in nitrogen atmosphere with a heating rate of 5 °C min^{-1}. The as-obtained black powders were then immersed in diluted hydrofluoric acid solutions (aladdin, 40 wt.% in H_2O) under stirring for 24 h, and then washed with anhydrous ethanol and deionized water, resulting in the formation of Ni_3Fe@HPC-CNT. The Ni@HPC-CNT and Fe@HPC-CNT were also prepared with only involvement of $Ni(NO_3)_2 \cdot 6H_2O$ or $Fe(NO_3)_3 \cdot 9H_2O$ as the metal source.

Preparation of Ni_3Fe@HPC-CNT modified Separator: The modified separator was fabricated by conventional doctor blade method. Briefly, 80 wt% Ni_3Fe@HPC-CNT, 10 wt% acetylene black and 10 wt% polyvinylidene fluoride (PVDF) was manually grinded in N-methyl-2-pyrrolidone (NMP) to form the slurry. Then, the slurry was coated onto the pristine separator (Celgard 2500) and dried at 80 °C in an oven for 12 h. The obtained Ni_3Fe@HPC-CNT modified separator was cut into discs with a diameter of 19 mm. The areal loading of Ni_3Fe@HPC-CNT coating layer is about 0.3 mg cm^{-2}. For comparison, Ni@HPC-CNT modified separator, Fe@HPC-CNT modified separator and PP separator without coating layer were also used as the comparison separators in Li-S batteries. In addition, to exclude the effect of carbon in the composite, acetylene black-carbon nanotube (AC) modified separator was also fabricated, which contains 80 wt% acetylene black, 10 wt% carbon nanotube and 10 wt% PVDF.

Preparation of Pure Sulfur Cathodes: For the cathode with a sulfur loading of ~1.5 mg cm^{-2} with a diameter of 12 mm, 70 wt% sulfur, 20 wt% acetylene black and 10 wt% PVDF were mixed in NMP to form a slurry, which was then coated on the carbon coated aluminum foil as cathode and dried at 60 °C for one night. Other than low sulfur loading cathode, the high sulfur loading cathodes (18.3 and 30 mg cm^{-2}) were prepared by titration method. Initially, 90 wt% sulfur and 10 wt% conductive carbon were ultrasonically dispersed in 10 mL NMP for 2 h. Then, the as-prepared mixture solutions were dripped into the carbon fiber and dried at 60 °C for 24 h. The different sulfur loadings in Li-S batteries were determined by adjusting the dripping volume of mixture solutions.

Preparation of Ni_3Fe@HPC-CNT/S cathodes: The battery performance of Li-S battery using S/Ni_3Fe@HPC-CNT cathode with pristine separator was investigated. The S/Ni_3Fe@HPC-CNT cathodes were prepared by melting-diffusion method. The Ni_3Fe@HPC-CNT and sulfur were mixed with a mass ratio of 2:3 and ground in mortar, sealing in a glass vial and heat under 155°C for 12 h. Then, the obtained S/Ni_3Fe@HPC-CNT composite, acetylene black and PVDF were well mixed with a mass ratio of 8:1:1 in NMP to form the slurry. The composite electrodes were fabricated by coating the slurry on carbon coated aluminum foil with a mass loading of ~1 mg cm^{-2}. The lithium disk was used as counter electrode while the Celgard 2500 was used as separator. 1.0 M LiTFSI + 2.0 wt% $LiNO_3$ dissolved in DOL/DME (V/V = 1:1) solvent used as the electrolytes. For comparison, AC/S cathodes were also fabricated via the above method.

Visualized adsorption experiments: The Li_2S_6 solutions were prepared by dissolving a mixture of sulfur and lithium sulfides (Li_2S) with a stoichiometric ratio of 5:1 in 1, 2-dimethoxyethane (DME), and then continuously stirring for 48 h at 60 °C in the glove box. The concentration of Li_2S_6 solutions was controlled at 5 mM. The Ni_3Fe@HPC-CNT, Fe@HPC-CNT, Ni@HPC-CNT and AC powders with same weight of 10 mg were then added into the 2 mL Li_2S_6 solutions, respectively. To sufficient adsorb the Li_2S_6 solutions, the above-mentioned mixture solutions were stirred for 24 h and then standing for 12 h for the UV-visible absorption experiments.

Assembly of Li_2S_6 symmetric cells: To assemble symmetrical cells, 1 M bis(trifluoroethanesulfony)imide lithium (LiTFSI) with 0.2 M Li_2S_6 in DME/DOL solutions (V/V = 1:1) was used as electrolytes, and the mixture of Ni_3Fe@HPC-CNT (or Fe@HPC-CNT, Ni@HPC-CNT, AC) and PVDF with a weight ratio of 9:1 as both the working electrode and counter electrode. The voltage range for cyclic voltammetry (CV) tests of symmetric cells was -1 to 1 V with a scan rate of 3 mV s^{-1}.

Li_2S nucleation measurements: The electrode was prepared by mixing active materials (Ni_3Fe@HPC-CNT or AC) and PVDF with a weight ratio of 9:1 in NMP solvent followed by coating the slurry onto the carbon coated aluminum foil. The Li_2S_8 solutions (0.2 M) were prepared by mixing Li_2S and S at a stoichiometric ratio of 1:7 in tetraglyme, with vigorous stirring for 24 h at 60 °C. Precipitation experiments of Li_2S on Ni_3Fe@HPC-CNT and AC were investigated in 2032-type coin cells with Celgard 2500 PP membrane as separator. 20 μL of Li_2S_8 (0.2 M) was dropped onto the cathode, the metal lithium was used as anode side. The cells were discharged galvanostatically to 2.06 V at 0.1 mA and then maintained potentiostatically at 2.05 V for the nucleation of Li_2S until the current dropped below 10^{-5} A. The nucleation capacity of Li_2S can be calculated by the integral area of the plotted curve through Faraday's Law.

Electrochemical Measurements: Electrochemical properties were investigated by using CR2032 coin-type cells, where the pure sulfur electrode applied as the cathode, lithium disk with a diameter of 16 mm worked as the anode (the thickness of lithium anode is 0.45 μm), the prepared modified separator served as the separator, and 1.0 M LiTFSI + 2.0 wt% $LiNO_3$ dissolved in DOL/DME (V/V = 1:1) solvent as the electrolytes. For the low sulfur cathode (~1.5 mg cm^{-2}), the amount of electrolytes used in Li-S battery was maintained at electrolyte/sulfur ratio of about 15 μL mg^{-1}. For the high sulfur cathode (18.3, 30 mg cm^{-2}), the amount of electrolytes used in Li-S battery was maintained at electrolyte/sulfur ratio of about 7 μL mg^{-1}. CV measurements and electrochemical impedance spectrometry (EIS) test were performed using AUTOLAB PGSTAT302N electrochemical workstation. The scan

rate and voltage range of CV measurements were 0.1 mV s^{-1} and 1.7-2.8 V, respectively. The EIS was studied at the open-circuit condition in a frequency range of 100 kHz to 10 mHz. The galvanostatic charge/discharge and rate performance tests were measured by CT2001A battery-test instrument with a voltage window of 1.7-2.8 V.

Ionic conductivity: The ionic conductivity of PP separator, Ni@HPC-CNT, Fe@HPC-CNT and Ni_3Fe@HPC-CNT modified separators was calculated from EIS using AUTOLAB PGSTAT302N electrochemical workstation. Either separator saturated with electrolyte was sandwiched between two stainless steel electrodes in coin cells, and its ionic conductivity was calculated according to the following equation:

$$\sigma = T/(R_0 S)$$

in which σ stands for ionic conductivity, T is the thickness of the membrane, S represents the area of the stainless steel electrode, and R_0 indicates the bulk Ohmic resistance of the electrolytes.

Li ion diffusion coefficient: The Li^+ diffusion coefficients were calculated by the Randles-Sevcik equation:

$$I_P = (2.69 \times 10^5) C_{Li}^{+} D_{Li}^{+\,1/2} A v^{1/2} n^{3/2}$$

Where I_P is the peak current, C_{Li}^{+} (mol mL^{-1}) is the Li^+ concentration in the electrolytes, D_{Li}^{+} is the Li^+ diffusion coefficient, A (cm^2) is the electrode area, v (V s^{-1}) is the scanning rate, and n (n = 2) stands the number of electrons in the redox reactions.

Materials Characterizations: X-ray diffraction (XRD) tests were carried out on a DX-2600 diffractometer with (Cu Kα radiation, λ = 1.5406 Å). Raman spectra were acquired on a LabRAM HR with 532 nm laser excitation. Field-emission scanning electron microscopy (FE-SEM), and transmission electron microscopy (TEM) equipped with energy dispersive X-ray spectroscopy (EDS) measurements were performed on the JSM-5900LV and FEI Talos F200x instruments, respectively. The specific surface area, pore volume and pore size distribution of the samples were measured by the N_2 adsorption-desorption isotherms at 77 K using a 30 Micromeritics ASAP 2020 equipment. The thermogravimetric (TG) experiments were performed on a TG-209F1 under air atmosphere with a heating rate

of 10 °C min^{-1}. Inductively coupled plasma-atomic emission spectrometry (ICP-AES) were measured on an Optima 4300DV. X-ray photoelectron spectroscopy analysis was performed on a PHI 5000 VersaProbe III with a monochromatic Al Kα X-ray source, with a base pressure better than 5×10^{-7} Pa. UV-vis spectra of the solutions were acquired on an ultraviolet and visible spectrophotometer (UV-3600). The Ni and Fe K-edge XAFS spectra were measured at beamline 17C1 of Taiwan Light Source and beamline 1W1B of Beijing Synchrotron Radiation Facility, The S K-edge XAFS spectra were measured at beamline 16A1 of Taiwan Light Source. The Ni and Fe L-edge XAFS spectra were measured at beamline 20A1 of Taiwan Light Source and beamline 02B02 of Shanghai Synchrotron Radiation Facility. The analysis of XAFS data was performed using the Athena software in Demeter package.

Calculation method: First principle DFT calculations were performed by the Vienna Ab initio Simulation Package (VASP)[1-2] with the projector augmented wave (PAW) method.[3] The exchange-functional was treated using the generalized gradient approximation (GGA) of Perdew-Burke-Ernzerhof (PBE)[4] functional. The energy cut off for the plane wave basis expansion was set to 400 eV and the force on each atom less than 0.05 eV/Å was set for convergence criterion of geometry relaxation. The self-consistent calculations applied a convergence energy threshold of 10^{-4} eV. The Brillouin zone integration was performed using 3×3×1 Monkhorst and Pack k-point sampling through all the computational process. Considering the van der Waals's interaction, Grimmes's method (DFT-D3)[5] was included during the surface adsorption.

$$E_{\text{ads}} = E_{X*} - E_X - E_*,$$

where X, *, and X* represents the adsorbate, substrate, and the adsorption system, respectively.

Climbing image nudged elastic band (Cl-NEB) method[6,7] has been used for finding saddle points and minimum energy paths of Li ion diffusion and the decomposition of Li_2S on the surface of composites.

The stability of different types of Ni-Fe alloy models are estimated by computing their formation energies (E_f) as

follows,

$$E_f = (E_{total} - n_{Ni}\mu_{Ni} - n_{Fe}\mu_{Fe} - n_C\mu_C)/N$$

where E_{total} can be obtained from the optimized calculation, n_{Ni}, n_{Fe}, and n_C are the numbers of Ni, Fe, and C atoms in the cell. N is the total number of these atoms. μ_{Ni}, μ_{Fe}, and μ_C are the chemical potentials of Ni, Fe, and C, respectively. To better simulate the experimental results, we have added a graphene layer on the surface of Ni, Fe, and Ni_3Fe.

Supplementary References:

[1] G. Kresse, J. Furthmüller, *Phys. Rev. B.* **1996**, *54,* 11169.

[2] G. Kresse, J. Furthmüller, *Comp. Mater. Sci.* **1996**, *6,* 15.

[3] P. E. Blöchl, *Phys. Rev. B.* **1994**, *50,* 17953.

[4] J. P. Perdew, K. Burke, M. Ernzerhof, *Phys. Rev. Lett.* **1996**, *77,* 3865.

[5] S. Grimme, J. Antony, S. Ehrlich, H. Krieg, *J. Chem. Phys.* **2010**, *132,* 154104.

[6] M. C. Prentiss, D. J. Wales, P. G. Wolynes, *Plos. Comput. Biol.* **2010**, *6*, e1000835.

[7] J. A. van den Ende, B. Ensing, H. M. Cuppen, *CrystEngComm* **2016**, *18,* 4420.

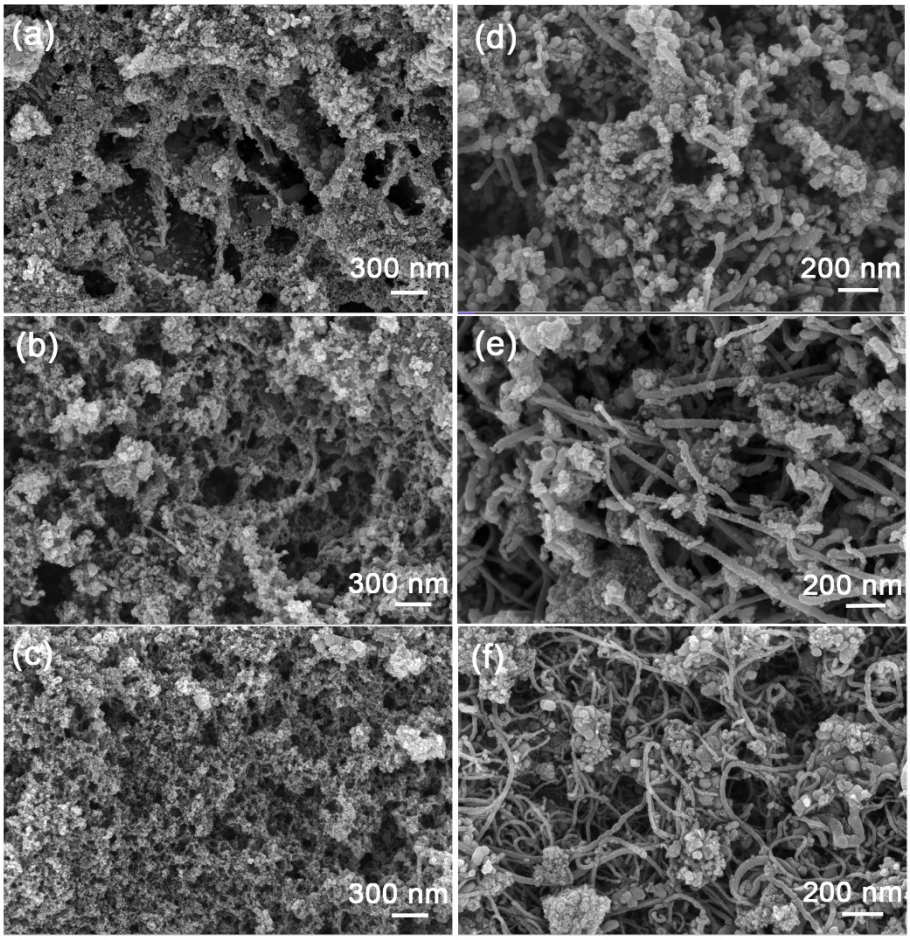

Figure S1. a, d) SEM images of Ni@HPC-CNT, b, e) Ni_3Fe@HPC-CNT and c, f) Fe@HPC-CNT under different magnifications.

As shown in Figure S1, Ni@HPC-CNT, Ni_3Fe@HPC-CNT and Fe@HPC-CNT samples exhibit a similar microstructure with three-dimensional interconnected porous framework with CNT in situ grown along the porous carbon.

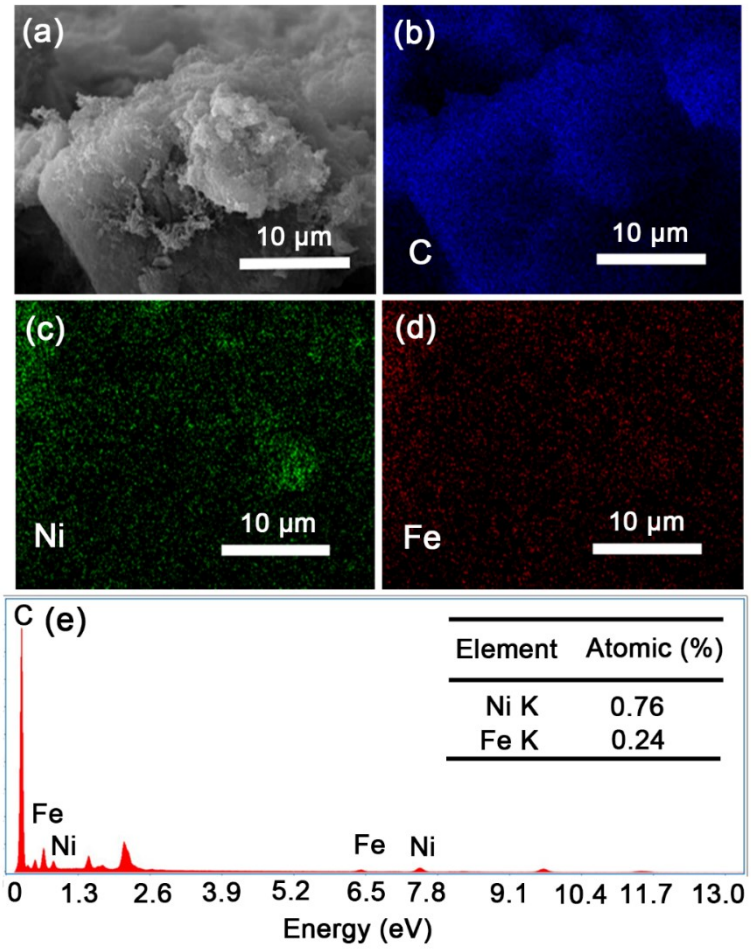

Figure S2. a) Field emission SEM image of Ni_3Fe@HPC-CNT and corresponding elemental mappings of b) C, c) Ni, and d) Fe. e) EDS spectrum of Ni_3Fe@HPC-CNT at a specific zone corresponding to Figure S2a.

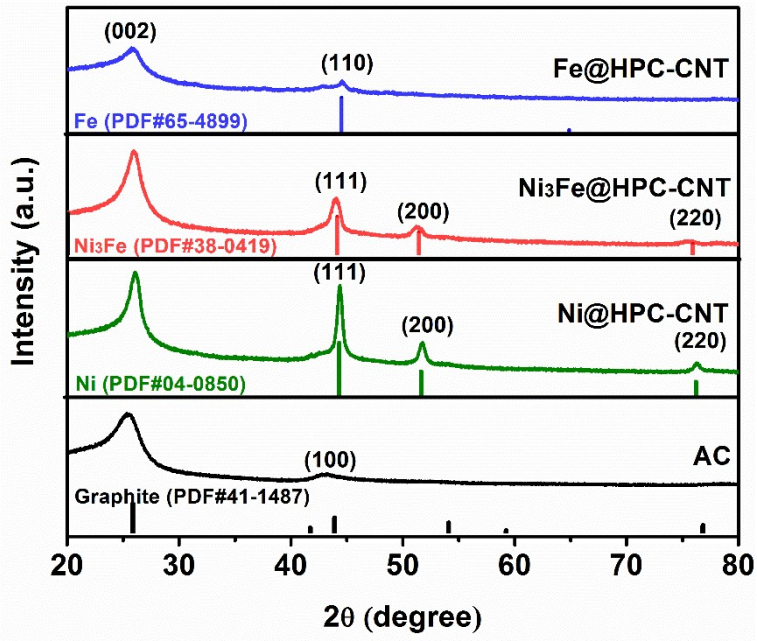

Figure S3. XRD patterns of AC and Ni-Fe samples (Ni@HPC-CNT, Ni_3Fe@HPC-CNT and Fe@HPC-CNT).

As shown in Figure S3, the Ni_3Fe@HPC-CNT sample exhibits three diffraction peaks at 44.2°, 51.5° and 75.3°, respectively, corresponding to the (111), (200) and (220) facets of Ni_3Fe alloy (PDF#38-0419). The intense diffraction peak at 26.4° is attributed to the (002) plane of graphitic carbon (PDF#41-1487). Furthermore, the Ni@HPC-CNT and Fe@HPC-CNT exhibit the pure Ni and Fe phases, respectively, accompanied with graphitic carbon phase.

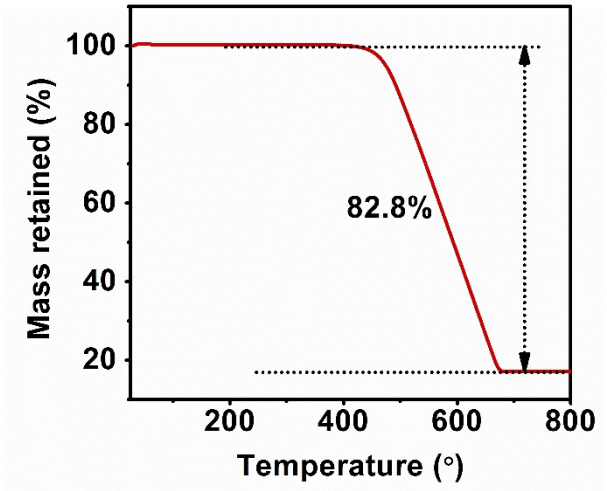

Figure S4. Thermogravimetric curve of Ni_3Fe@HPC-CNT under air atmosphere.

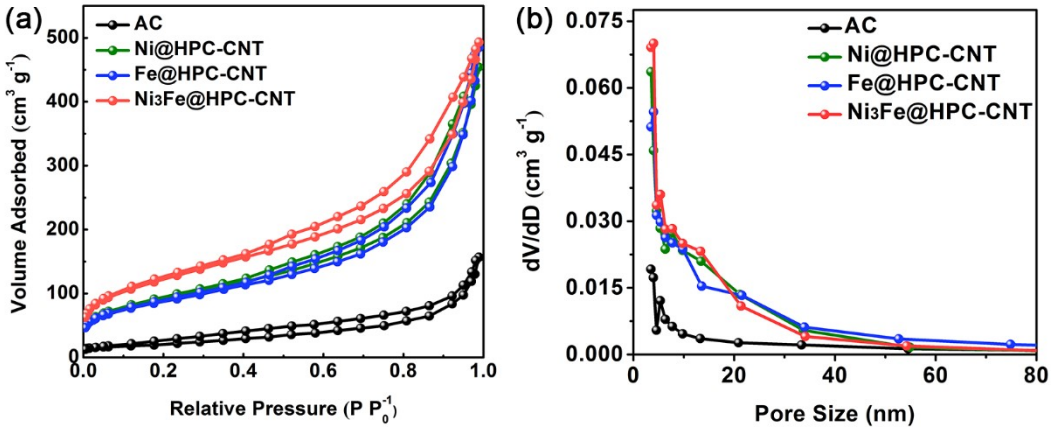

Figure S5. a) Nitrogen physisorption isotherms and b) corresponding pore-size distributions of the AC, Ni@HPC-CNT, Fe@HPC-CNT and Ni_3Fe@HPC-CNT.

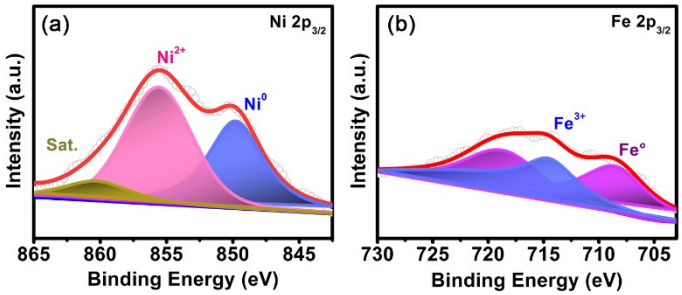

Figure S6. XPS spectra of a) Ni $2p_{3/2}$ and b) Fe $2p_{3/2}$ for Ni_3Fe@HPC-CNT.

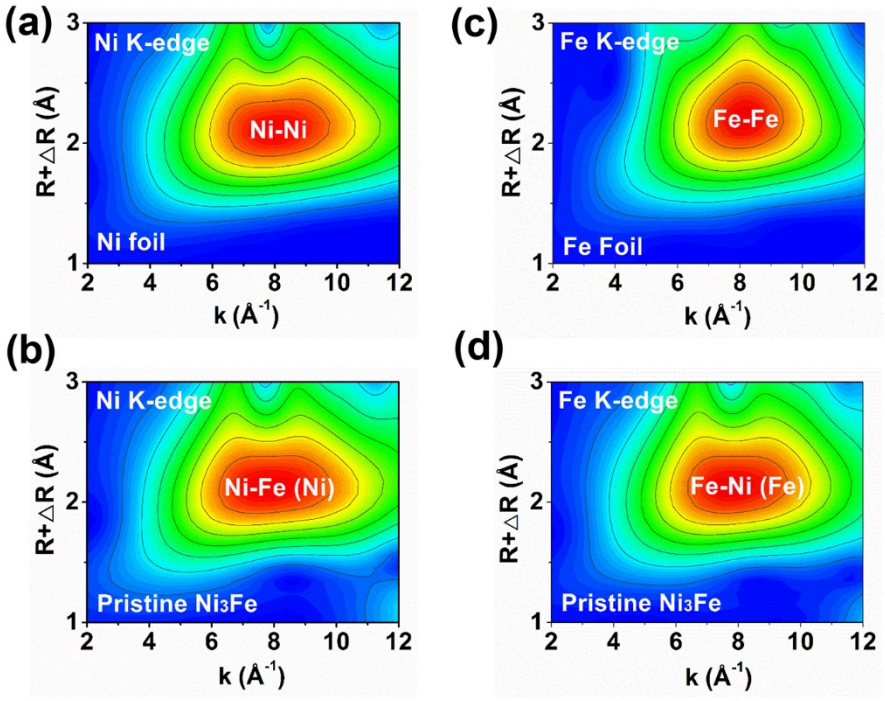

Figure S7. WT transform contour plots of a, b) Ni and c, d) Fe K-edge.

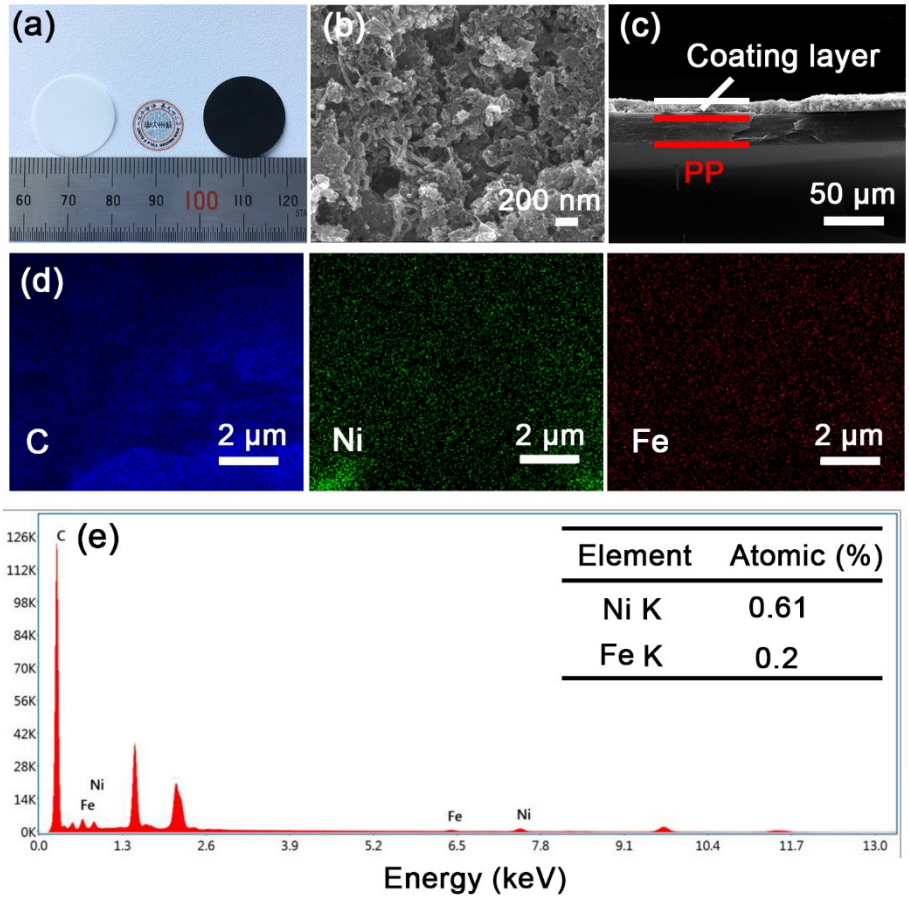

Figure S8. a) Photograph of the Ni_3Fe@HPC-CNT modified separator. b) Top view and c) cross-sectional SEM images of the Ni_3Fe@HPC-CNT modified separator. d) Elemental mappings and e) EDS image of Ni_3Fe@HPC-CNT modified separator corresponding to the blue box area in Figure S8c.

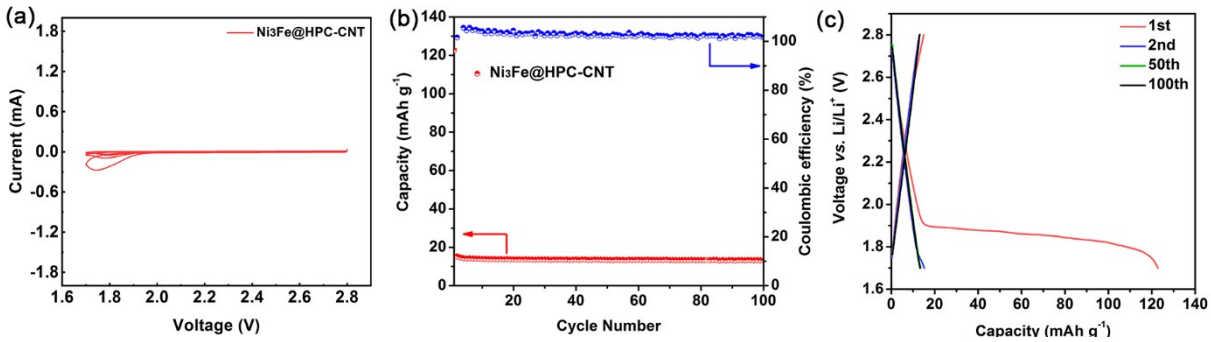

Figure S9. a) CV curves of Ni_3Fe@HPC-CNT cathode without sulfur in voltage window of 1.7-2.8 V. b) Cycle performance and c) charge/discharge profiles of pure Ni_3Fe@HPC-CNT cathode at 180 mA g^{-1} after first cycle at 90 mA g^{-1}.

As seen in Figure 2a, an additional cathodic peak at ~1.8 V is observed in Ni-Fe modified separator batteries, whereas no cathodic peak at ~1.8 V can be detected in PP and AC separator batteries. This phenomenon implies that the cathodic peak at ~1.8 V is associated with metals in the modified separators. To reveal the origin of cathodic peak at 1.8V and estimate the capacity contribution of Ni_3Fe alloy, the batteries with Ni_3Fe@HPC-CNT as the cathode (without sulfur) and lithium as the anode are assembled and tested under similar conditions. As seen in Figure S9, when using Ni_3Fe@HPC-CNT cathode without sulfur, the typical cathodic peaks at 2.3 and 2.0 V as well as anodic peak at 2.4 V are disappeared. However, a small cathodic peak at around 1.8 V is still observed. This result suggests that the origin of cathodic peak at 1.8V derives from the partial lithiation of Ni_3Fe alloy. Meanwhile, from the charge/discharge curves, the capacity of Ni_3Fe@HPC-CNT is as low as 14 mAh g^{-1}, which can be neglected when compared with the high special capacity (1675 mAh g^{-1}) of sulfur.

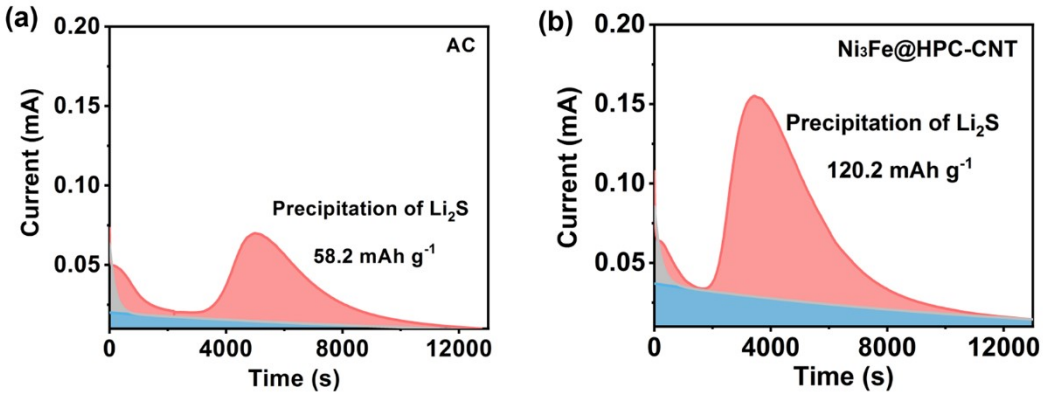

Figure S10. Potentiostatic discharge curves of Li_2S_8 solution on the surface of (a) AC and (b) Ni_3Fe@HPC-CNT electrode at 2.05 V.

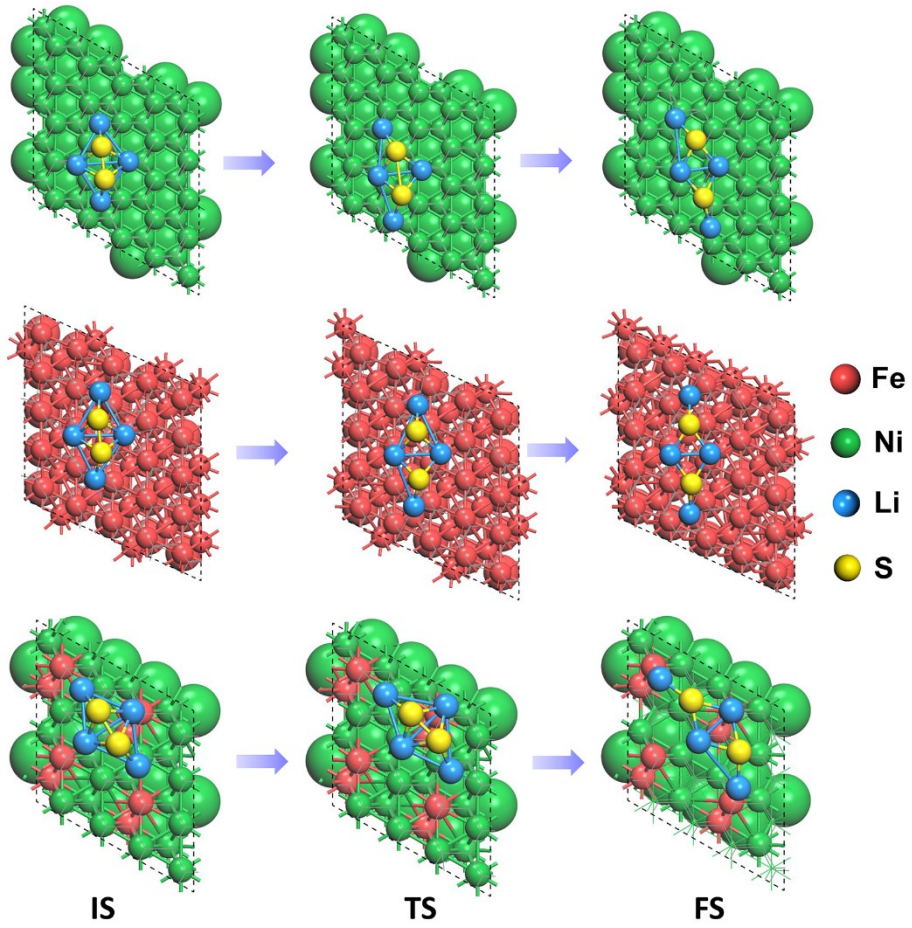

Figure S11. Initial state (IS), transition state (TS), and final state (FS) of Li_2S_2 decomposition on the Ni, Fe and Ni_3Fe surface.

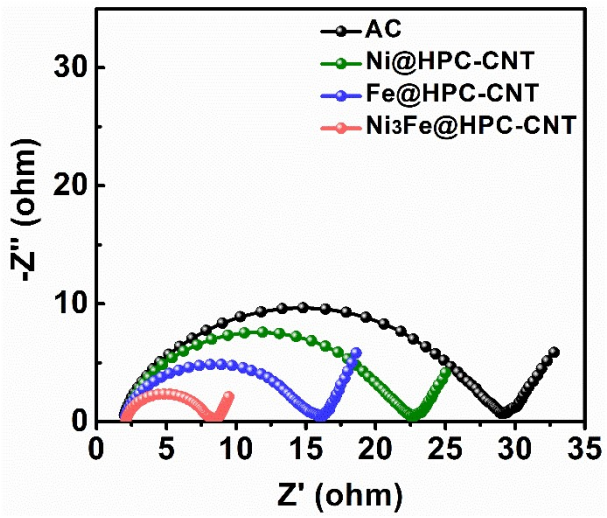

Figure S12. EIS spectra of Li_2S_6 symmetric cells using AC, Ni@HPC-CNT, Fe@HPC-CNT and Ni_3Fe@HPC-CNT electrodes.

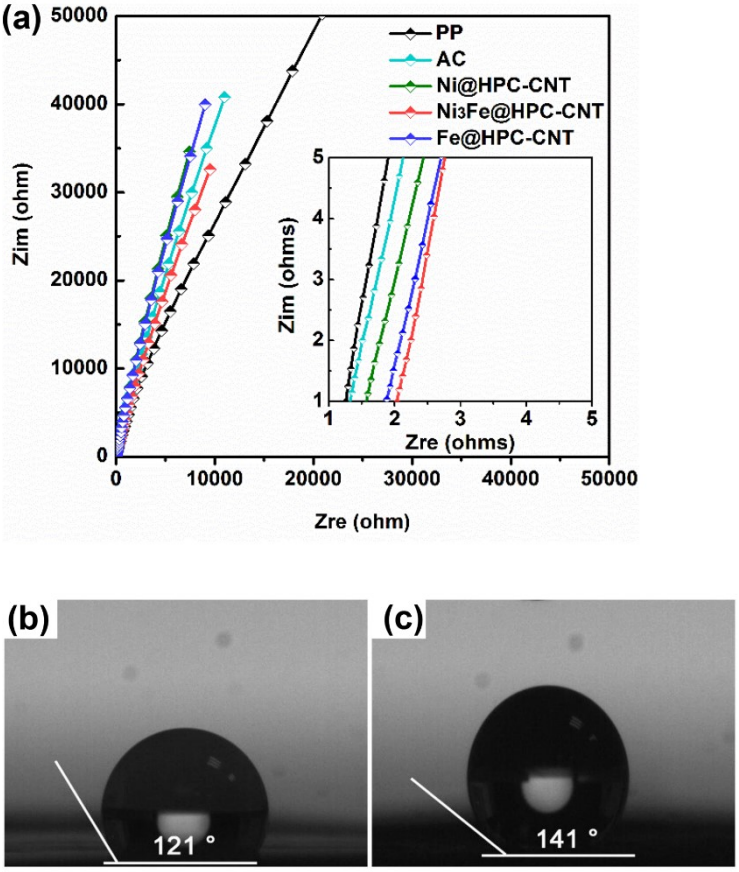

Figure S13. a) EIS plots of the symmetrical steel plate coin cells using different separators. Inset is the enlarged EIS plots at the high-frequency region. Contact angel of Ni_3Fe@HPC-CNT modified separator b) and PP separator c) with electrolytes.

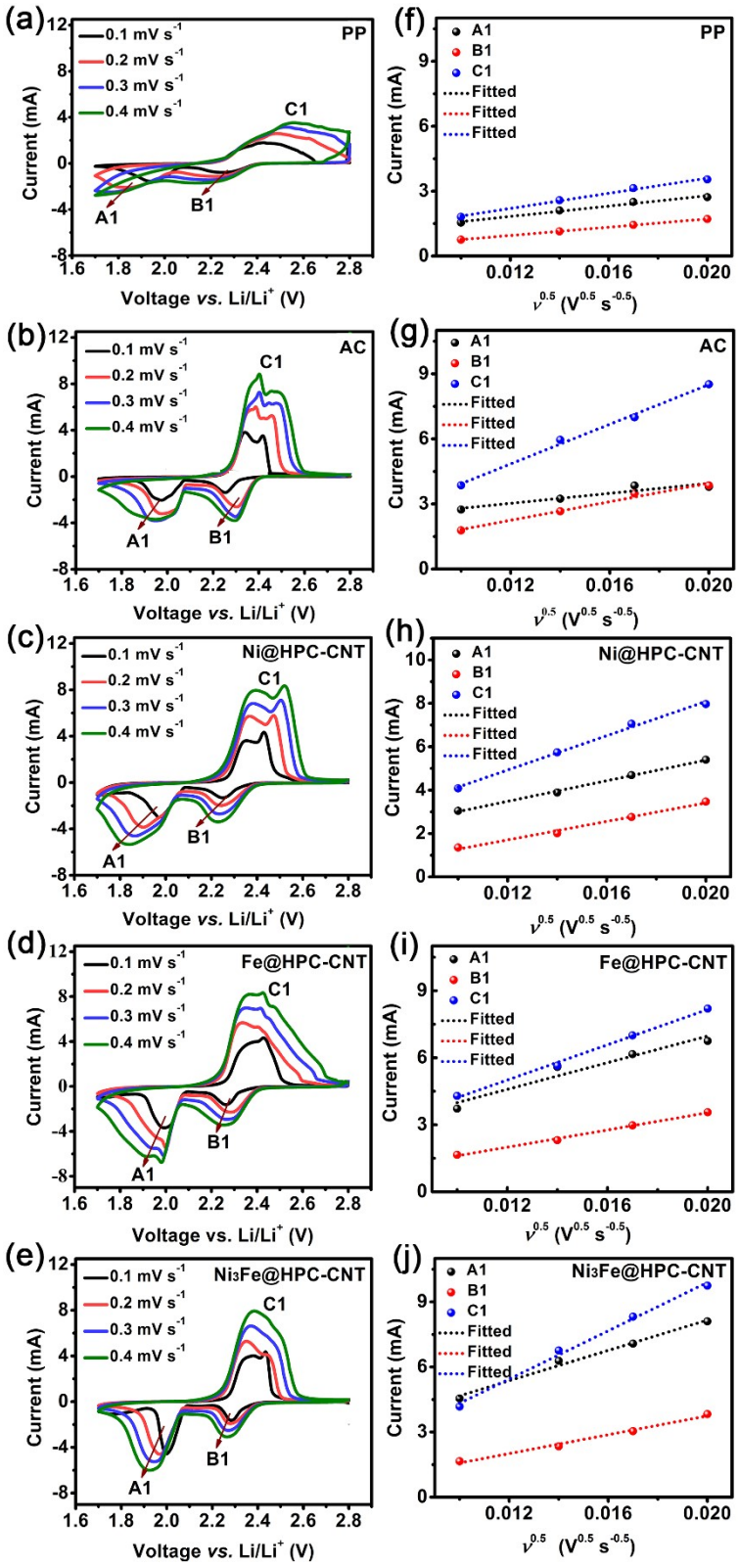

Figure S14. a-e) CV curves of Li-S batteries with different separators at various scan rates and f-j) corresponding linear fits of the redox peak currents.

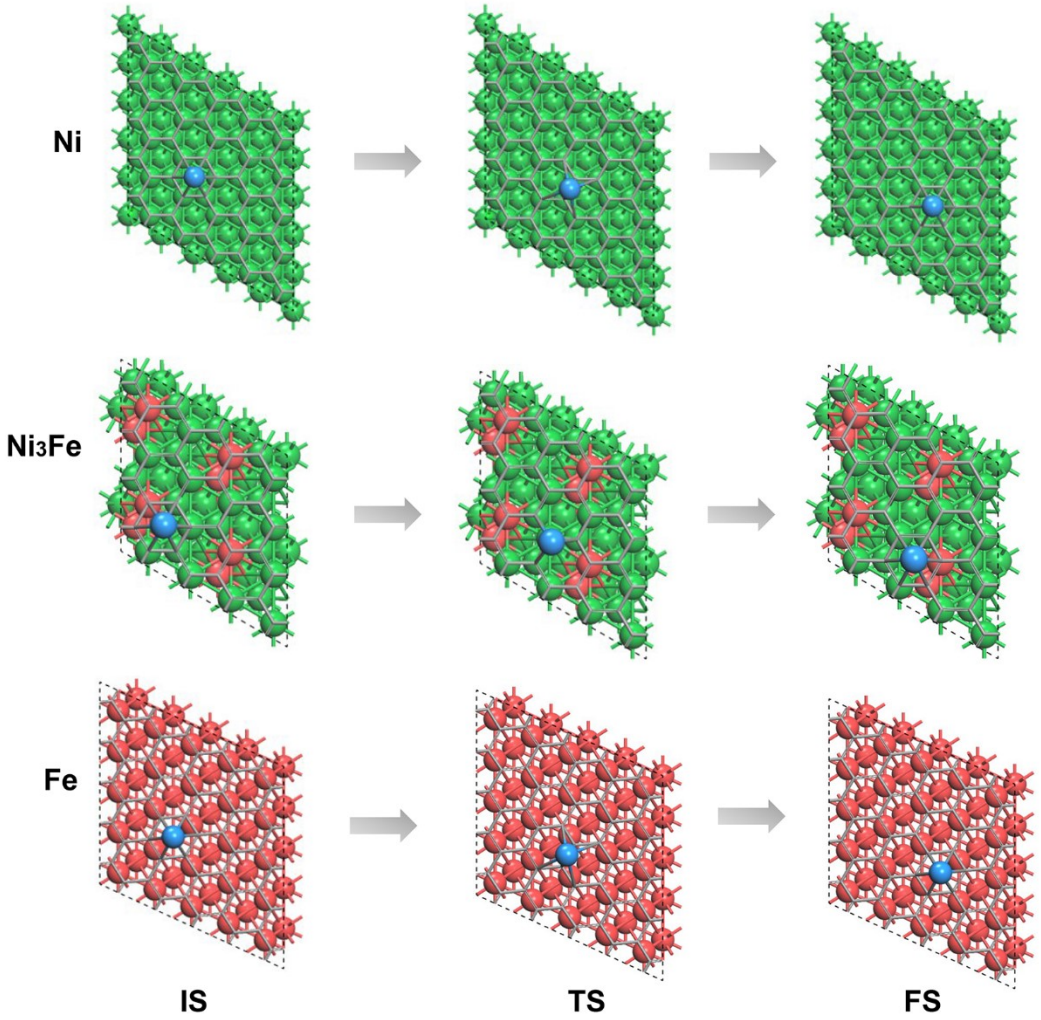

Figure S15. Initial state (IS), transition state (TS), and final state (FS) of Li^+ diffusion on different surfaces.

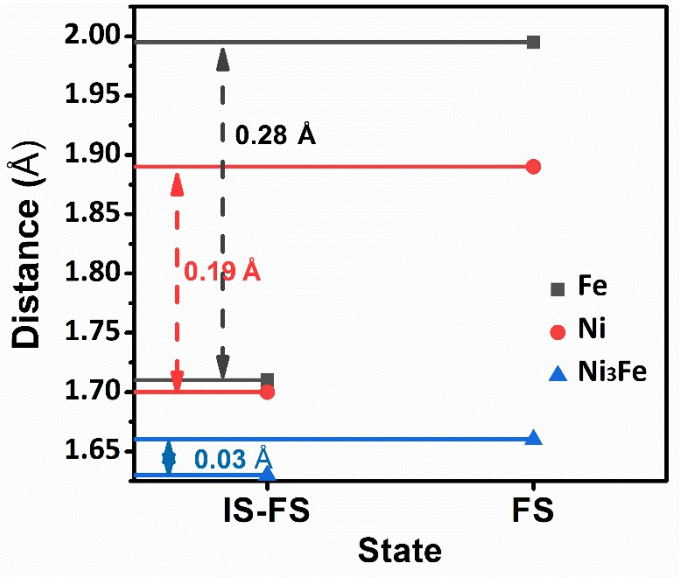

Figure S16. Distances between Li^+ and metal surface from disposal direction during the diffusion process.

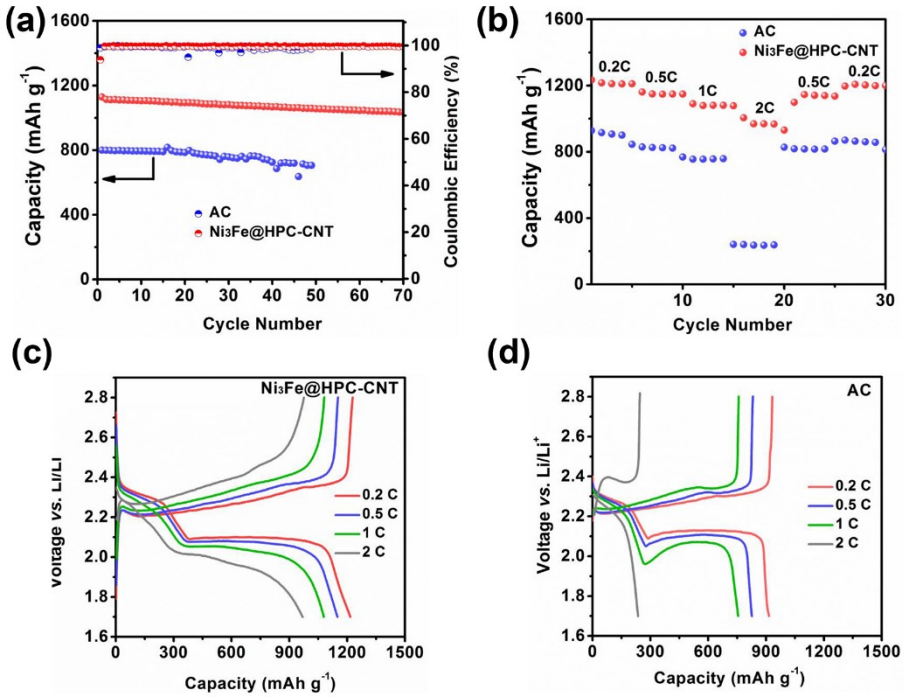

Figure S17. a) Cycle performance of Ni_3Fe@HPC-CNT/S and AC/S cathodes at 0.5 C. b) Rate performance of Ni_3Fe@HPC-CNT/S and AC/S cathodes from 0.2 C to 2 C. The corresponding charge/discharge curves of c) Ni_3Fe@HPC-CNT/S and d) AC/S cathodes at various rates.

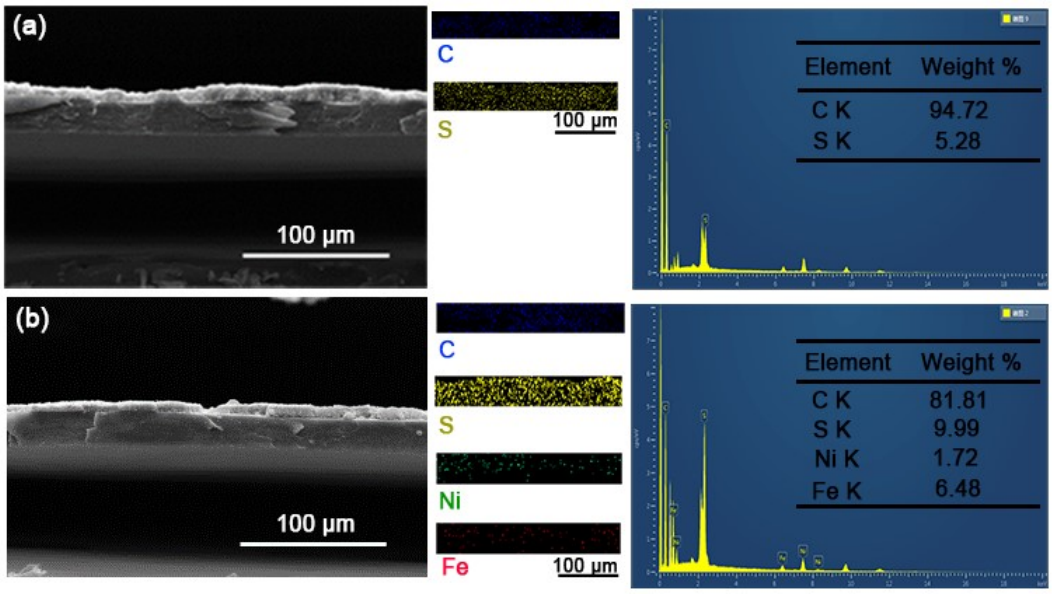

Figure S18. Cross-sectional SEM images, corresponding EDS and elemental mappings of a) AC modified separator and b) Ni_3Fe@HPC-CNT modified separator after 800 cycles at 2 C.

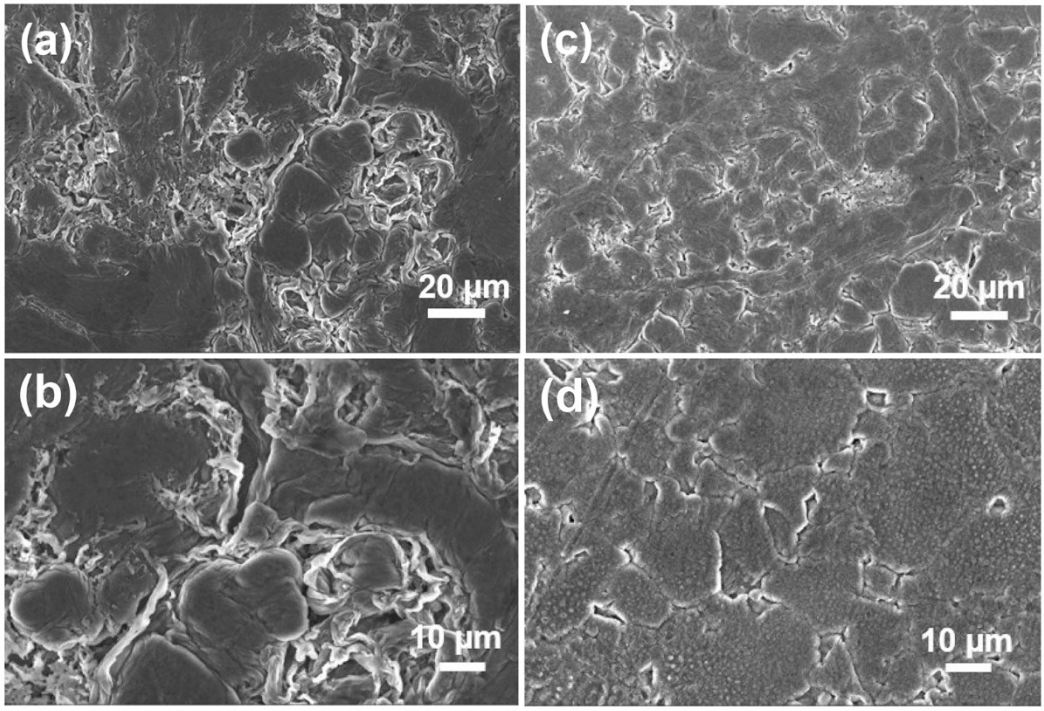

Figure S19. SEM images of the Li anodes for Li-S batteries using a, b) AC and c, d) Ni_3Fe@HPC-CNT modified separators after 800 cycles at 2 C.

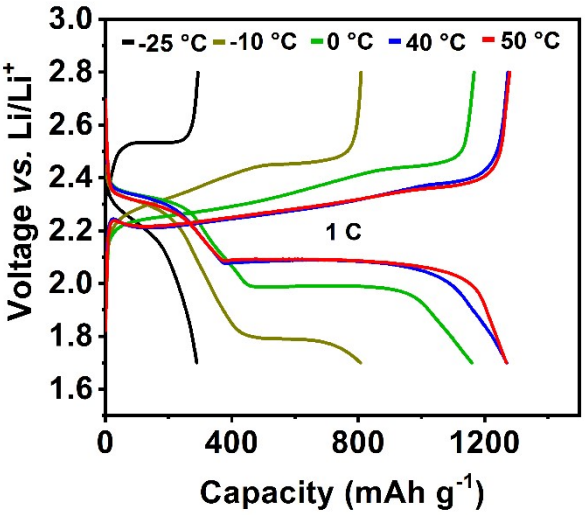

Figure S20. Charge/discharge curves of Li-S battery with Ni_3Fe@HPC-CNT modified separator at 1 C from -25 °C to 50 °C.

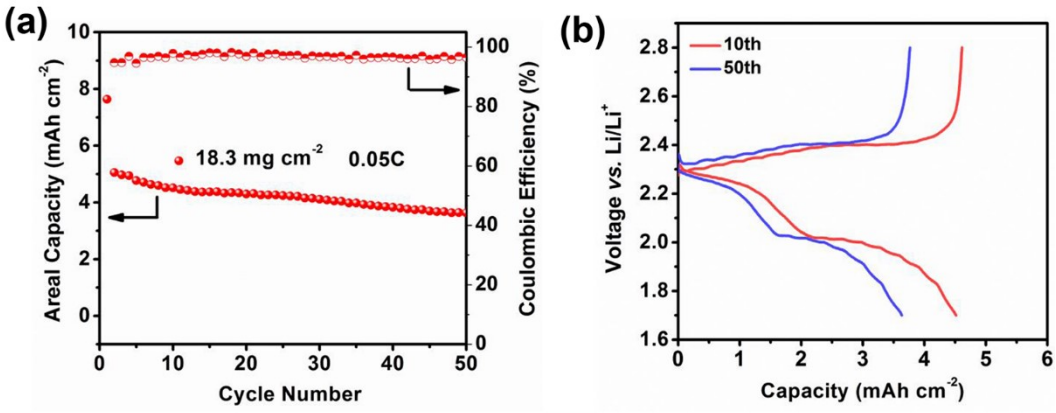

Figure S21. a) Cycling performance and b) charge/discharge curves of Ni_3Fe@HPC-CNT/S cathode with pristine separator under high sulfur loadings and low E/S ratio of approximately 7 μL mg^{-1} at 0.05 C.

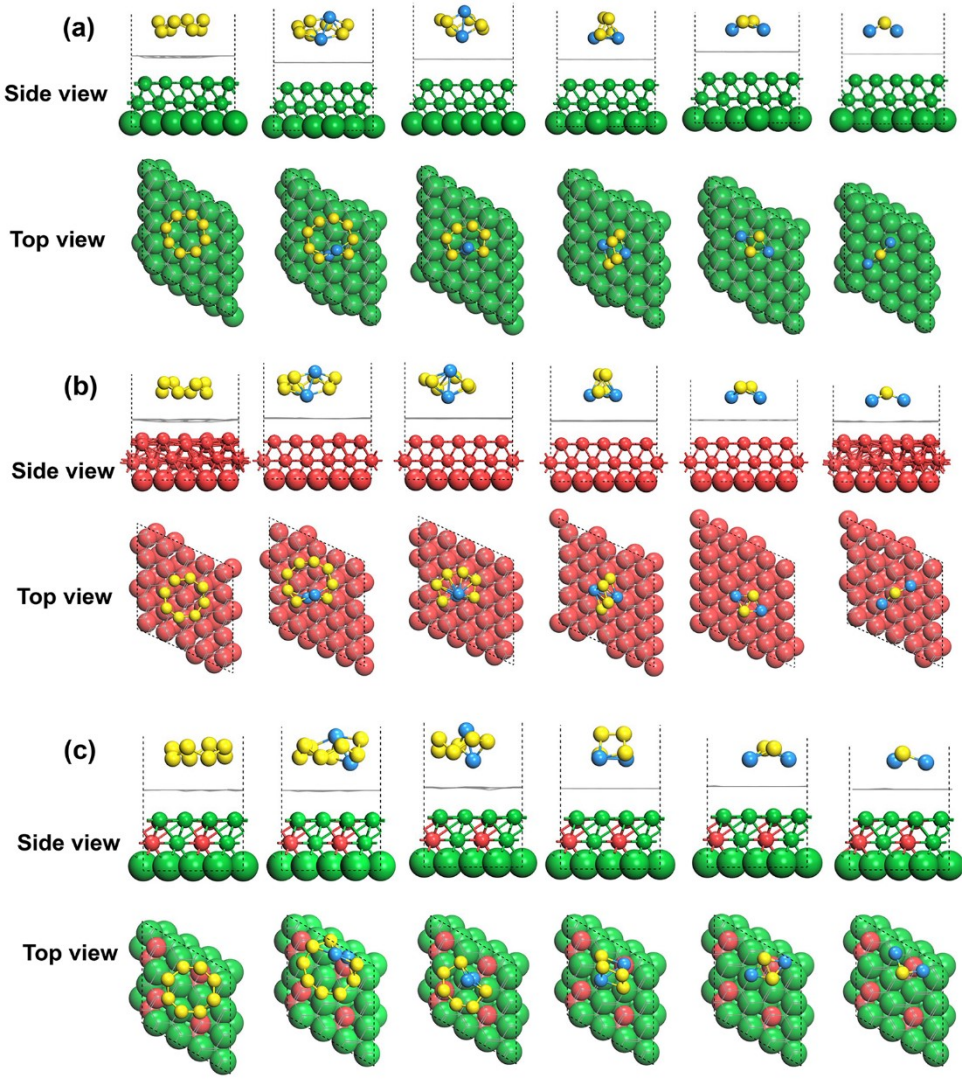

Figure S22. Optimized geometrical structures of S_8 and Li_2S_x (x = 1, 2, 4, 6 or 8) adsorbed on the a) Ni, b) Fe and c) Ni_3Fe.

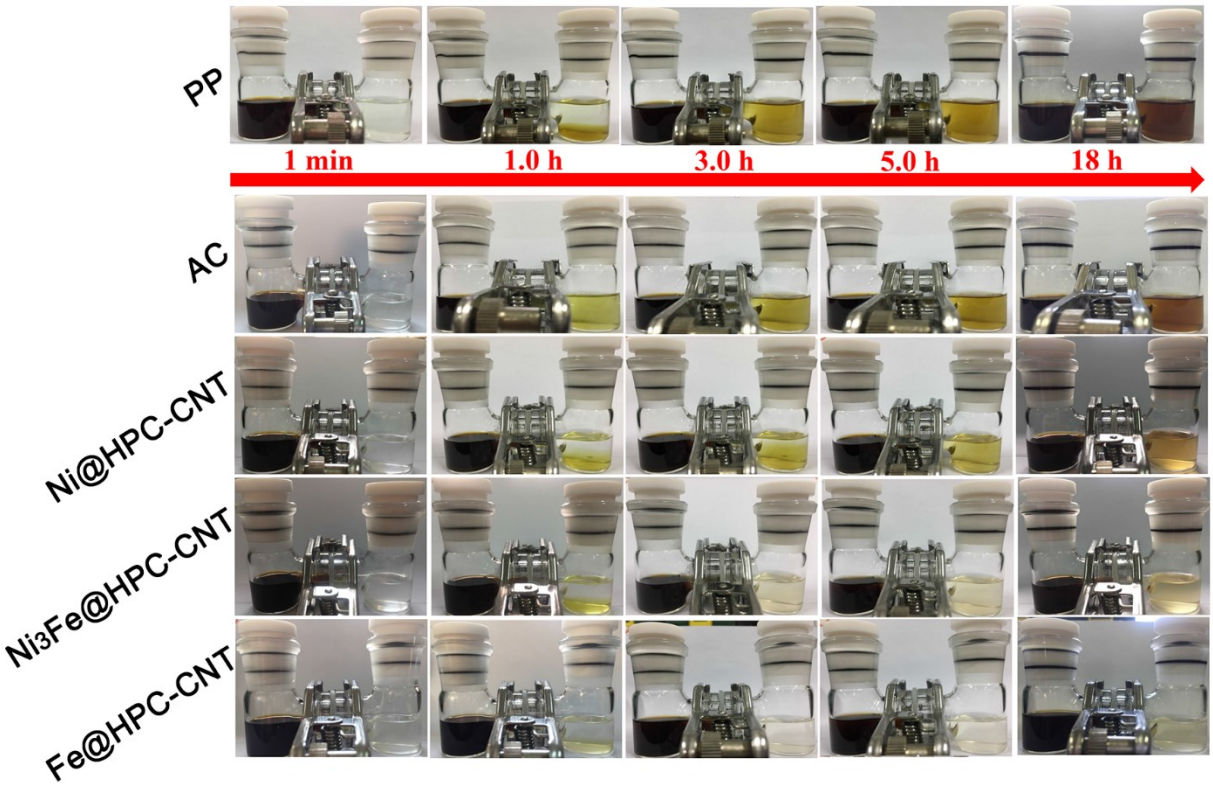

Figure S23. Polysulfide diffusion in H-type cells with different separators.

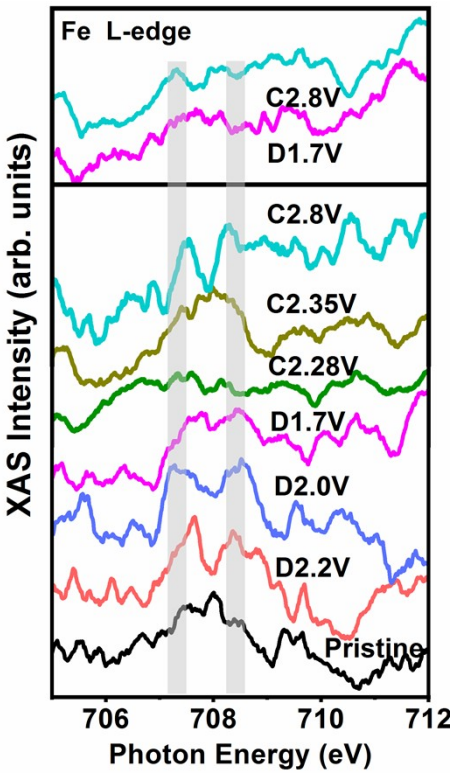

Figure S24. Fe L-edge XANES spectra of Ni_3Fe@HPC-CNT modified separators at different charge/discharge states and cycles.

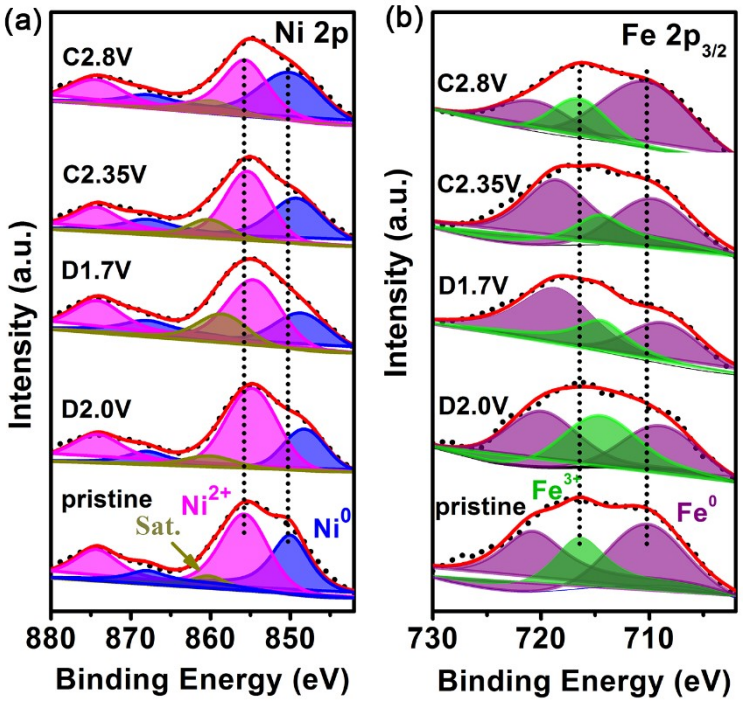

Figure S25. XPS spectra of a) Ni 2p and b) Fe $2p_{3/2}$ of Ni_3Fe@HPC-CNT modified separator at different charge/discharge states.

Table S1. ICP-AES results of Ni_3Fe@HPC-CNT sample.

Element	Ni	Fe
Mass ratio (%)	8.53	3.56

Table S2. BET specific surface area for all the compared samples.

Samples	BET surface area (m^2 g^{-1})	Pore volume (cm^3 g^{-1})
AC	65	0.24
Ni@HPC-CNT	230	0.70
Ni_3Fe@HPC-CNT	227	0.75
Fe@HPC-CNT	253	0.76

Table S3. The Li^+ conductivity of various separators.

Samples	Li^+ conductivity [mS cm^{-1}]
PP separator	1.82×10^{-2}
CNT modified separator	1.69×10^{-2}
Ni@HPC-CNT modified separator	1.39×10^{-2}
Ni_3Fe@HPC-CNT modified separator	1.14×10^{-2}
Fe@HPC-CNT modified separator	1.08×10^{-2}

Table S4. Summary of the Li^+ diffusion coefficient for Li-S batteries with different separators.

Samples	D_{Li^+} [$cm^2\ S^{-1}$]		
	A_1 Peak	B_1 Peak	C_1 Peak
PP	1.94×10^{-8}	1.24×10^{-8}	4.13×10^{-8}
AC	1.78×10^{-8}	6.19×10^{-8}	2.82×10^{-7}
Ni@HPC-CNT	6.42×10^{-8}	4.68×10^{-8}	3.77×10^{-7}
Fe@HPC-CNT	1.2×10^{-7}	5.04×10^{-8}	2.11×10^{-7}
Ni_3Fe@HPC-CNT	1.65×10^{-7}	6.37×10^{-8}	4.19×10^{-7}

Table S5. Bader charge of Li^+ on Fe, Ni and Ni_3Fe surface during the diffusion process.

	IS-FS/e	TS/e	Charge difference/e
Fe/Gra	0.126	0.110	0.016
Ni/Gra	0.132	0.108	0.024
Ni_3Fe/Gra	0.130	0.111	0.019

Because Li^+ need climb only 0.03 Å on Ni_3Fe surface, and 0.19/0.28 Å on Ni /Fe surface during the diffusion process. The high distance for Ni and Fe indicates a strong bonding energy to overcome, which can be improved from the change of bader charge on adsorbed Li^+ (Table S6).

Table S6. Electrochemical properties of various functional separators in Li-S batteries at room-temperature.

References	Coating materials	Sulfur content (wt%)	Mass loading of the coating (mg cm^{-2})	Cycle Performance			Rate Performance
				Initial capacity (mAh g^{-1})	Rate (C)	Capacity decay (%)	
[4] ***ACS nano*** 2020, 14, 9819.	D-HVS	70	0.14	1156	0.2 C	0.072 (300th)	630 (2 C)
[5] ***ACS Appl. Mater. Interfaces*** 2020, 12, 19572.	Ni_3Fe@NCNT	70	0.2	895	1 C	0.034 (1000th)	598 (4 C)
[6] ***Adv. Energy Mater.*** 2018, 8, 1801778.	LNS/CB	70	0.7	1198	0.2 C	0.06 (500th)	758 (2 C)
[8] ***J. Mater. Chem. A*** 2018, 6, 14359.	MTN	70	--	1032	0.2 C	0.09 (400th)	672 (3 C)
[9] ***ACS Energy Lett.*** 2017, 2, 2362.	ZIF-7	63	1.2	1025	0.25 C	0.19 (300th)	452 (2.5 C)
[41] ***ACS Nano*** 2018, 12, 836-843	ZBCP/GF/CNT	63	--	1272	0.25 C	0.209 (200th)	610 (2.5 C)
[42] ***Adv. Funct. Mater.*** 2016, 26, 7817.	$BaTiO_3$	60	2.4	1122	0.5 C	0.34 (50th)	300 (3 C)
[43] ***Adv. Mater.*** 2017, 29, 1606817.	MoS_2	65	--	808	0.5 C	0.083 (600th)	550 (1 C)
[37] ***Adv. Mater.*** 2019, 31, e1903813.	SC-Co	63	0.3	1130	0.5 C	0.086 (300th)	805 (3 C)
[44] ***ACS Nano*** 2018, 12, 2381.	MXene (Ti_3C_2)	49	0.4	899	0.5 C	0.266 (200th)	288 (10 C)
[38] ***Energy Environ. Sci.*** 2018, 11, 2560.	Co_9S_8	70	0.16	869	1 C	0.039(1000th)	428 (2 C)
[39] ***Chem. Comm.*** 2020, 56, 3007.	4Co-NCNTs	49	0.23	872.3	1 C	0.072 (700th)	664 (2 C)
[45] ***Nanoscale*** 2018, 10, 13694.	CoP nanospheres	70	0.2	928	1 C	0.078 (500th)	725 (5 C)
[46] ***Nano Energy*** 2019, 59, 390.	Super P/RP	65	0.3	890	1 C	0.18 (500th)	809 (2 C)
[47] ***ACS nano*** 2017, 11, 2697.	CNTs/V_2O_5 RSL	50	0.4-0.6	1068	1 C	0.05 (250th)	614 (4 C)
[48] ***Adv. Energy Mater.*** 2018, 8. 1702288	MWCNTs/NCQDs	60	0.15	1331	1 C	0.05 (500th)	666.7 (3 C)
[3] ***Matter*** 2019, 1,	Li*x*Mo_6S_8	54	0.4	1056	1 C	0.07 (400th)	728 (4 C)

1047.							
[22] ***Adv. Mater.*** 2020, 32, e1904876.	Sb_2Se_{3-x}	56	0.5	975	1 C	0.027 (500th)	787 (8 C)
[49] ***ACS Nano*** 2019, 13, 1923.	Ce-MOF/CNT	--	0.4	1022	1 C	0.02 (800th)	663 (4 C)
[50] ***Chem. Eng. J.*** 2018, 349, 327.	HNPC	70	0.36	915	1 C	0.06 (900th)	674 (2 C)
[51] ***Adv. Mater.*** 2020, 32, e1906722.	MOF-Co	56	--	800	1 C	0.07 (600th)	478 (5 C)
[52] ***Adv. Mater.*** 2019, 31, e1903955.	Ni@NG	--	0.3	1059	1 C	0.06 (500th)	612 (10 C)
[53] ***Chem. Sci.*** 2017, 8, 6619.	TiO-C65	60	0.7	1047	2 C	0.16 (300th)	800 (1 C)
[54] ***ACS Nano*** 2018, 12, 10240.	NHG	61.2	0.1	868	2 C	0.06 (800th)	987 (2 C)
[55] ***Adv. Mater.*** 2016, 28, 9551.	LDH/NG	63	0.3	812	2 C	0.06 (1000th)	709 (2 C)
[56] ***Chem. Eng. J.*** 2020, 381, 122701.	Co/NCNS/CNT	64	0.2	972	2 C	0.05 (1000th)	842 (2 C)
[57] ***Adv. Funct. Mater.*** 2018, 28, 1706513.	LiF/GO	64	0.15	721	2 C	0.043 (400th)	524 (3 C)
[12] ***Adv. Energy Mater.*** 2019, 9, 1901609.	Co-N_xNPC/G	60	0.2	964	2 C	0.087 (500th)	801 (5 C)
[20] ***Adv. Mater.*** 2020, 32, e1907444.	OVs-TiO_2	66.7	0.12	802	2 C	0.043 (500th)	751 (3 C)
This work	**Ni_3Fe@HPC-CNT**	**70**	**0.3**	**1120**	**2 C**	**0.05 (800th)**	**800 (10 C)** **645 (15 C)**

Table S7. Comparison of the low-temperature performance of Li-S batteries with representative work.

References	Cathode	Separator	Temperature (°C)	Rate performance (mAh g^{-1})			Cycle Performance (mAh g^{-1})
				0.5 C	1 C	2 C	
[58] ***Nano Energy*** 2013, 2, 314.	PGS-1000	PP	**-20**	360	--	234	175 (80th, 1C, -20 °C)
[15] ***ACS Nano*** 2018, 12, 11120.	BN/Graphene-S	PP	**0** **-20** **-40**	738 669 401	-- -- --	-- -- --	500 (300th, 1C, -20 °C)
[13] ***Adv. Energy Mater.*** 2018, 1703638.	rGO-$MoSe_2$	PP	**0** **-25**	-- --	779 272	-- --	538 (500th, 0.5C, 0 °C) 253 (500th, 0.5C, -25 °C)
[14] ***Adv. Energy Mater.*** 2020, 2000907.	Ni@C/graphene	PP	**-40** **-50**	--	-- --	-- --	354 (200th, 0.1C, -40 °C) 274 (400th, 0.1C, -50 °C)
This work	Pure S	Ni_3Fe@HPC-CNT	**0** **-10** **-25**	-- -- --	**1166** **920** **294**	**1038** **420** **225**	-- 476 (400th, 0.5C, -10 °C) --

Table S8. Comparison of areal capacities of high-loading cathodes between this work and other literatures.

References	Cathode	separator	Sulfur content	Sulfur mass loading (mg cm^{-2})	Current density	Initial capacity (mAh cm^{-2})	End capacity (mAh cm^{-2})
[5] ***ACS Appl. Mater. Interfaces*** 2020, 12, 19572.	super P/S	Ni_3Fe@NCNT	70%	7.7	0.2 C	5.3	4.3 (150th)
[4] ***ACS nano*** 2020, 14, 9819.	Super P/S	D-HVS	70%	9.2	0.2 C	8. 3	6 (120th)
[42] ***Adv. Funct. Mater.*** 2016, 26, 7817.	EC/S	$BaTiO_3$	60%	3	0.5 C	3.4	2.8 (50th)
[22] ***Adv. Mater.*** 2020, 32, e1904876.	CNT/S	Sb_2Se_3	56%	8.1	0.1 C	7.5	6.6 (100th)
[20] ***Adv. Mater.*** 2020, 32, e1907444.	rGO/S	OVs-TiO_2	80%	7.1	0.2 C	6.7	5.83 (100th)
[51] ***Adv. Mater.*** 2020, 32, e1906722.	C/S	MOF-Co	56%	7.8	0.5 C	7.8	5 (200th)
[11] ***ACS nano*** 2020, 14, 11558.	C/S	Co_7Fe_3@PGC-CNT	70%	6.7	0.1 C	6.5	4.7 (90th)
[47] ***ACS nano*** 2017, 11, 2697.	Carbon black/S	CNTs/V_2O_5 RSL interlayer	70.4%	6	0.1 C	7.94	4.5 (100th)
[59] ***Nano Energy*** 2019, 64, 103905.	rGO@S	NiCo-CNF@CF	56%	8	0.1 C	7.04	~5.8 (50th)
[60] ***ACS nano*** 2019, 13, 13235.	VTe_2@MgO/S	PP	60%	6.9	0.1 C	6.5	4.3 (50th)
[61] ***Matter*** 2020, 2, 1-16.	eGF@S	PP	80%	20	~0.1 C	21	19 (70th)
[62] ***ACS nano*** 2019, 13, 14208.	Fe/Co−N@C/S	PP	70%	6.5	0.1 C	8.7	~6.4
[63] ***Energ. Environ. Sci.*** 2018, 11, 2620.	VO_2-VN/S	PP	61.8%	13.2	0.05 C	~8.3	5.7 (20th)
[64] ***Adv. Mater.*** 2016, 28, 3374.	HCFF-S	PP	76%	21.2	0.05 C	23.2	14.8 (150th)
In this work	CF/S	Ni_3Fe@HPC-CNT	-- 70%	**18.3** **30**	0.05 C 0.05 C	**17.3** **25.5**	**15 (50th)** **16 (50th)**

Note: Taking the mass of the carbon fiber into account, the sulfur content is 70% for the Li-S battery using Ni_3Fe@HPC-CNT modified separator.

Table S9. Peak intensity ratios (A_2/B_2) of the Ni L-edge for the Ni_3Fe@HPC-CNT.

Potentials	Intensity Ratios (A_2/B_2)
Before discharging	0.91
Discharge to 2.2 V	0.94
Discharge to 2.0 V	0.99
Discharge to 1.7 V	0.99
Charge to 2.28 V	0.97
Charge to 2.35V	0.97
Charge to 2.8 V	0.96